



**HAL**  
open science

## Optical Enantioseparation of Racemic Emulsions of Chiral Microparticles

Nina Kravets, Artur Aleksanyan, Hamza Chraibi, Jacques Leng, Etienne Brasselet

► **To cite this version:**

Nina Kravets, Artur Aleksanyan, Hamza Chraibi, Jacques Leng, Etienne Brasselet. Optical Enantioseparation of Racemic Emulsions of Chiral Microparticles. *Physical Review Applied*, 2019, 11 (4), 10.1103/PhysRevApplied.11.044025 . hal-02104123

**HAL Id: hal-02104123**

**<https://hal.science/hal-02104123>**

Submitted on 19 Apr 2019

**HAL** is a multi-disciplinary open access archive for the deposit and dissemination of scientific research documents, whether they are published or not. The documents may come from teaching and research institutions in France or abroad, or from public or private research centers.

L'archive ouverte pluridisciplinaire **HAL**, est destinée au dépôt et à la diffusion de documents scientifiques de niveau recherche, publiés ou non, émanant des établissements d'enseignement et de recherche français ou étrangers, des laboratoires publics ou privés.

# Optical Enantioseparation of Racemic Emulsions of Chiral Microparticles

Nina Kravets,<sup>1</sup> Artur Aleksanyan,<sup>1</sup> Hamza Chraïbi,<sup>1</sup> Jacques Leng,<sup>2</sup> and Etienne Brasselet<sup>1,\*</sup>

<sup>1</sup>*Université de Bordeaux, CNRS, LOMA, UMR 5798, Talence F-33400, France*

<sup>2</sup>*Université de Bordeaux, CNRS, Solvay, LOF, UMR 5258, Pessac 33608, France*

 (Received 7 September 2018; revised manuscript received 28 November 2018; published 9 April 2019)

We report on the experimental demonstration of chirality-selective mechanical separation of randomly distributed assemblies of right-handed and left-handed chiral microparticles by optical means. Chiral-resolution experiments are made using two-dimensional emulsions of chiral-liquid-crystal droplets under the action of circularly polarized laser beams and do not require information on the initial location of the particles. Also, we numerically identify that the cooperative effects of hydrodynamic interactions mediated by the viscous fluid surrounding the particles can speed up the enantioseparation process.

DOI: [10.1103/PhysRevApplied.11.044025](https://doi.org/10.1103/PhysRevApplied.11.044025)

## I. INTRODUCTION

The property characterizing an entity that is not superimposable on its mirror image—chirality—is an old concept that was experimentally articulated by Pasteur in the 19th century, in the framework of his optical studies [1], the name itself being introduced by Kelvin several decades later [2]. Chirality is a geometric concept that plays a role across scientific disciplines. In particular, its central place in the universal question about the origin of life [3] makes it a property of Nature, the appeal of which is timeless and reaches out to the general public. In fact, chiral substances are part of our everyday life as, for instance, active compounds such as drugs and cosmetics. The sought-after effect of a chiral molecule, however, may crucially depend on its handedness, while the usual synthesis techniques do not lead to only one of the two enantiomers (i.e., the mirror-image versions of a chiral compound). This implies the need for postsynthesis chirality-selective techniques to resolve racemic (i.e., equal weights) mixtures of two enantiomers. The spontaneous chiral resolution during crystallization demonstrated by Pasteur is a famous example; however, such processes remain restricted only to a small fraction of the chiral species [4,5]. Although established chiral-resolution techniques [6,7] operate at the industrial scale, further developments are to be welcomed, especially toward the elaboration of compound-insensitive processes.

The search for alternative techniques based on chirality-selective interaction between chiral entities and external physical fields (electric, magnetic, optical, electronic, etc.) is a longstanding issue [8]. In particular, it was recognized early on that asymmetric light-matter processes can

be directed by the photon helicity by favoring one of the two enantiomers as the product of a phototransformation, such as in photolysis [9], photoresolution [10], and photosynthesis [11]. Intriguingly, the establishment of a chirality-selective optomechanical sorting processes is a topic that has emerged only recently, with the aim at replacing the visual recognition process and hand-made tweezers of Pasteur with passive all-optical processes. Despite ever-increasing theoretical efforts from many groups to establish the foundations of this challenging topic (see, e.g., Refs. [12–29]), there are only a few experimental reports to date that deal with discriminatory effects for single chiral microparticles at a time [30–35].

Here, we report on an experimental attempt to resolve a racemic assembly of chiral particles by purely optical means. The experimental observations are made by choosing chiral-liquid-crystal (cholesteric) droplets arranged into a two-dimensional emulsion. The sorting time as a function of the size of the particle is discussed and calls for the need for a boosted light-induced chiral discriminatory drift for submicrometer particles. Numerical investigations reveal the boosting role of hydrodynamic interactions in the chiral-resolution process, which is assessed for two-dimensional (2D) and three-dimensional (3D) racemic emulsions.

## II. THE EXPERIMENTAL APPROACH

Monodisperse droplets of right-handed and left-handed chiral liquid crystals are prepared by microfluidic techniques [36]. In our case, we use a polydimethylsiloxane (PDMS, Sylgard 184) chip enabling droplet generation by a pinch-off mechanism (see Fig. 1). Note that in order to make an oil-in-water emulsion in a PDMS chip, the

\*[etienne.brasselet@u-bordeaux.fr](mailto:etienne.brasselet@u-bordeaux.fr)

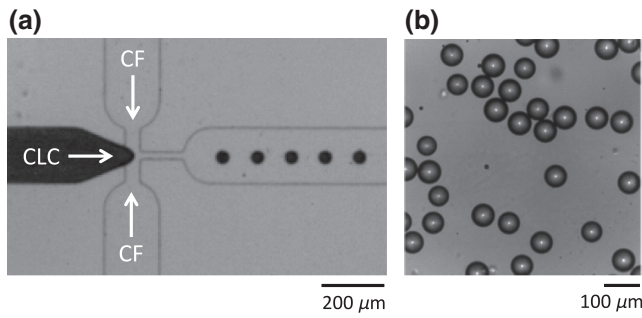


FIG. 1. (a) A top-view bright-field snapshot of the microfluidic device: CLC, cholesteric liquid crystal; CF, carrier fluid. The channel nozzle dimensions are  $40 \mu\text{m} \times 50 \mu\text{m}$  and the output channel width and height are  $200 \mu\text{m}$  and  $50 \mu\text{m}$ , respectively. (b) A bright-field image of the generated monodisperse emulsion.

latter is surface treated with a Mirapol Surf S 500 polymer mixture to make it hydrophilic. The carrier fluid is approximately 30 wt% aqueous glycerol mixture, doped with approximately 2 wt% polyvinyl alcohol. The use of glycerol allows us to reduce the viscosity contrast between the carrier fluid and provides us with an almost isodense droplet mixture. This eases the fabrication and handling of the emulsions. In addition, the use of a small fraction of polyvinyl alcohol prevents the coalescence of droplets.

We use two cholesteric-liquid-crystal (CLC) commercial mixtures from BEAM Co., characterized by a molecular helical arrangement of the liquid-crystal molecules with same pitch  $p$  and opposite helix handedness [Fig. 2(a)]. These CLC mixtures are prepared by doping the nematic HB443 liquid crystal with the right- and left-twisting chiral dopants CHD-56624-R and CHD-56624-S (all being BEAM Co. products) and fine tuning their concentrations to obtain the design's Bragg wavelength. Cholesterics are well known to exhibit a strong chirality-selective circular Bragg reflection phenomenon [37] that refers to discriminatory reflection of circularly polarized light, provided that the optical electric field helix and the material helix are cohanded. This is illustrated in Fig. 2(b), where the co- and contrahanded reflection spectra are shown for both right-handed and left-handed cholesteric planar films using the same materials as those used to prepare the droplets, for which the chirality-selective reflection band is designed to be centered close to  $\lambda_0 = 532 \text{ nm}$  that is the wavelength of the laser light field used for sorting.

The carrier fluid used promotes parallel anchoring of the liquid-crystal molecules at the surface of the droplets. In turn, our droplets are characterized by a radial distribution of the helix axis [38] (see also Ref. [39] for a numerical description of the fine 3D molecular ordering). The observed circular Bragg reflection phenomenon is qualitatively the same as for planar films. However, the 3D confinement brings a substantial complexity to

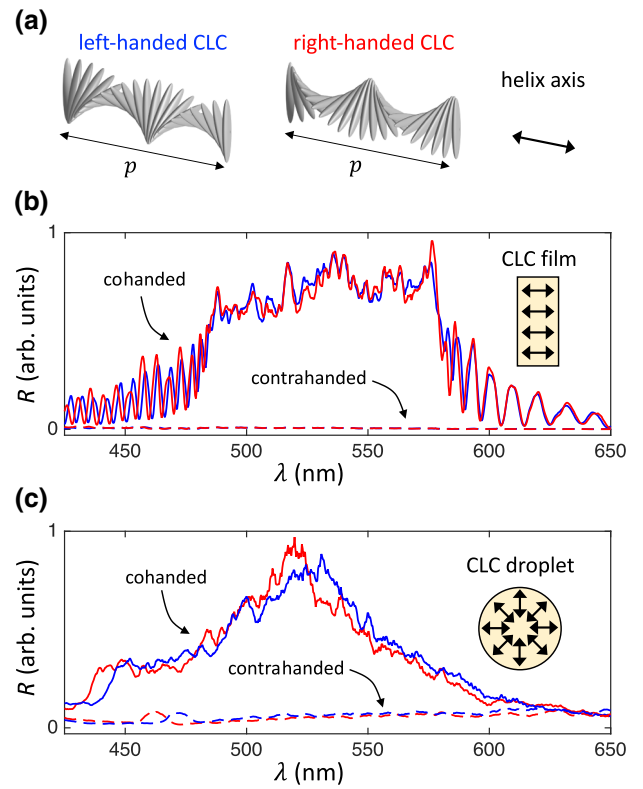


FIG. 2. (a) An illustration of the helical ordering of the liquid-crystal molecules for left-handed and right-handed materials. The helix axis is depicted as a two headed arrow. (b) Reflection spectra at normal incidence of cholesteric films confined between two parallel glass substrates separated by a  $8 \mu\text{m}$  gap and providing in-plane homogeneous orientational boundary conditions, measured both for cohanded (solid lines) and contrahanded (dashed lines) optical and material helices. The blue and red colors refer to the material helix handedness, as shown in panel (a). (c) Reflection spectra for droplets with a radius of  $30 \mu\text{m}$ . Spectra for films and droplets are recorded at room temperature using a supercontinuum laser source and a fiber spectrometer. Every spectrum is the average of five independent measurements and is normalized by the spectrum obtained from the Fresnel reflection from a bare glass substrate.

the structure itself and the ensuing light-matter interaction, which remains to be properly addressed theoretically. From an experimental point of view, even the reflection spectra of individual chiral Bragg droplets have not yet been reported, despite these objects motivating practical applications in photonics, such as self-assembled omnidirectional microlasers [40]. Here, we report on the experimental assessment of such missing spectral information, as shown in Fig. 2(c), for generated droplets having a radius  $R_0 = 30 \mu\text{m}$ . As shown in Fig. 2(c), the cohanded spectra are less top-hat shaped than for films, while the contrahanded spectra remain flat. Strong discriminatory optical behavior is obtained at  $\lambda_0$ .

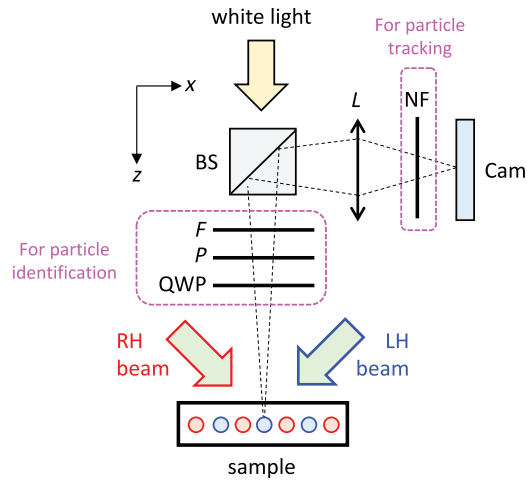


FIG. 3. A sketch of the experimental setup for all-optical chiral resolution: P, polarizer; BS, beam splitter; QWP, quarter-wave plate; F, spectral filter at 532 nm wavelength, with 10 nm full width at half maximum transmission peak; L, lens; Cam, camera; LH, left-handed; RH, right-handed; NF, notch filter, selectively rejecting the scattered laser light at 532 nm. The sample is a sealed chamber with a thickness of approximately  $200 \mu\text{m}$  and an area of approximately  $2 \text{ cm}^2$ , filled with a racemic mixture of left-handed and right-handed droplets.

Equal volumes of independently prepared emulsions of left-handed and right-handed droplets generated by the microfluidic device are mixed and placed between two glass substrates separated by an approximately  $200 \mu\text{m}$  gap. The sample is placed horizontally to discard the effect of gravity (see the setup sketch in Fig. 3). Spectrally filtered polarized halogen illumination is used to identify and tag the handedness of individual droplets. Indeed, according to Fig. 2(c), the reflective co-handed circularly polarized imaging of the droplets gives bright images, whereas dark images are obtained in the contrahanded situation [see Fig. 4(a)]. The droplets are further irradiated by two continuous-wave Gaussian beams with wavelength  $\lambda_0$  at a  $45^\circ$  angle of incidence. The two collimated Gaussian beams are mutually contracircularly polarized, have the same optical power  $P$  and same beam radius  $\sim 500 \mu\text{m}$  defined as the distance from the beam axis where the intensity falls by a factor  $\exp(-2)$ . Their intensity cross sections in the observation plane of the sample are shown in Fig. 4(b). Hydrophilic surface treatment is carried out to prevent the droplet from wetting the bottom glass substrate, hence improving the robustness of the experiments. The sorting experiments are carried out at approximately  $10^\circ\text{C}$  above room temperature in order to optimize the optomechanical response of the droplet. The latter point is explained by the importance of the location of the driving-beam wavelength  $\lambda_0$  inside the circular Bragg photonic band gap [31], noting that the temperature allows fine tuning of the spectral location of the band gap.

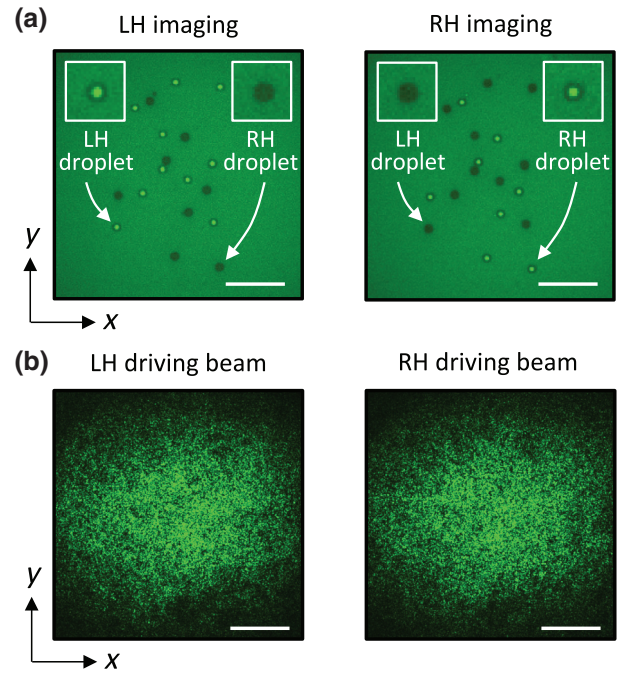


FIG. 4. (a) Direct optical identification of the chirality of every droplet of the used racemic emulsion of droplets via reflective incoherent circular polarization imaging while the two laser beams are off (rotation of the QWP by  $90^\circ$  allows switching between LH and RH reflections). (b) Observation of the elliptically shaped intensity cross sections in the observation plane for the two driving beams, which is done by placing a tracing paper inside the mixture in which the droplets are immersed. Scale bars:  $500 \mu\text{m}$ .

### III. 2D CHIRAL OPTICAL SORTING EXPERIMENTS

The principle of all-optical chiral resolution basically relies on the discriminatory optical force exerted by the two driving laser beams on the droplets. Indeed, it is known that a circularly polarized wave illuminating a chiral-liquid-crystal droplet exerts on it a force that depends strongly on the relative optical and material handedness, provided that the optical wavelength falls in the circular photonic band gap [31]. In addition, the latter force is directed along the propagation direction of the driving light field. Since the movement of the droplets is restricted here to the  $x$ - $y$  plane, the light-induced motion is qualitatively expected to take place along the  $x$  axis.

The chirality-selective displacement is ensured by the use of two contracircularly polarized beams [32]. An experimental demonstration is reported in Figs. 5(a) and 5(b), which show, respectively, the spatial distribution of the droplets at time  $t = 0$  at which the laser beams are switched on and after an irradiation duration of about 2 h under  $P = 2 \text{ W}$ , for which the maximal force-field magnitude  $F_0$  exerted on a droplet is of the order of a few

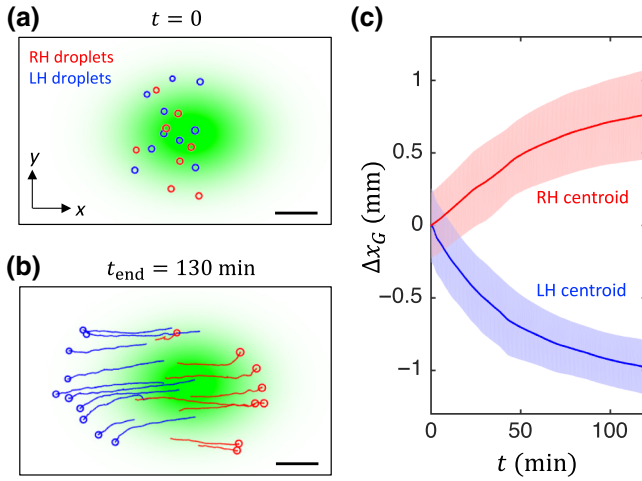


FIG. 5. An experimental demonstration of all-optical chiral resolution. (a) The initial spatial distribution of the droplets (circular markers), the handedness of which is identified according to the protocol illustrated in Fig. 4(a). (b) The location of the droplets after 130 min irradiation with  $P = 2$  W and individual trajectories. The Gaussian fit of the intensity cross section in the observation plane [see Fig. 4(b)], is shown in green. Scale bars:  $500 \mu\text{m}$ . (c) The dynamics along the  $x$  axis of the left-handed (LH) and right-handed (RH) droplet centroids, defined as  $\Delta x_G^{\text{RH,LH}}(t) = x_G^{\text{RH,LH}}(t) - x_G^{\text{RH,LH}}(0)$ , where  $x_G^{\text{RH,LH}} = (1/M_{\text{RH,LH}}) \sum_i x_i^{\text{RH,LH}}$ ,  $M_{\text{RH,LH}}$  being the total number of droplets of a given handedness and  $x_i^{\text{RH,LH}}$  being the  $i$ th droplet coordinate along the  $x$  axis.

piconewtons, according to [32]. The dynamics of the individual trajectories of the droplets are retrieved by processing the recorded video. The droplet motion mainly occurs along the  $x$  axis, as shown in Fig. 5(b). Quantitatively, the sorting dynamics is illustrated in Fig. 5(c), which presents the centroid dynamics for each chiral droplet population, unveiling a maximal velocity of the order of  $10 \mu\text{m min}^{-1}$ , which remains modest for practical implementation. The displacement asymptotically converges at the rim of the Gaussian beams as the optical intensity and hence the optical force exponentially decays to zero. As expected due to symmetry considerations, reversing the polarization state of both beams reverses the displacement direction of the droplets while preserving the chiral-resolution process.

Also, we note that the observed trajectories are curved and that their very nature depends on the event. This suggests that uncontrolled experimental side effects are at work. One can mention the possible role of the inhomogeneous surface state of the bottom substrate and the nonideally smooth Gaussian intensity profiles. Recalling that the orientation of the radial defect of the droplets [38] is uncontrolled, the detailed nature of the optomechanical effect itself should also be at play. Indeed, this is expected to lead to an optical scattering force, the direction of which depends on its orientation.

The size of the particles used here for proof-of-principle experimental demonstration is comparable to molecular crystals that researchers might want to sort in real-world applications; nevertheless, chiral particles with smaller sizes should be also considered. Accordingly, we discuss in the next section how the sorting time scales, and how much the entities are spread after the sorting, with respect to the size of the particle and the spatial extent of the initially racemic assembly.

#### IV. THE INFLUENCE OF PARTICLE SIZE AND THE INITIAL SIZE OF THE RACEMIC ASSEMBLY ON THE SORTING PROCESS

First, we address the scaling of the optical force with respect to the radius  $R$  of the particle. We consider a racemic particle assembly with initial spatial extent  $L_0$ , as sketched in Fig. 6(a), under the action of a uniform chiral discriminatory optical force field  $F_{\text{opt}}$ . We describe the particles as a collection of noninteracting spheres in linear translation in an unbounded Newtonian fluid with dynamic viscosity  $\eta$ . We account for a low Reynolds number, which is the case in practice. The right-handed and left-handed particle assemblies move in opposite directions at constant velocity and hence drift apart by a distance  $d_{\text{opt}} = (F_{\text{opt}}/(6\pi\eta R))t = \alpha t$  after an irradiation duration time  $t$ . Meanwhile, the Brownian motion leads each particle to explore a region with a typical time-dependent size defined by the Stokes-Einstein expression  $d_B = (k_B T/(3\pi\eta R))^{1/2} t^{1/2} = \beta t^{1/2}$ , where  $k_B$  is the Boltzmann constant and  $T$  is the temperature.

The radiation-pressure force originating from the circular Bragg reflection phenomenon scales with the surface of the effective spin-dependent mirror. In the case of spherical particles, it scales as  $R^2$  [31]. Thus one can obtain the following scaling laws with respect to the particle size:

$$d_{\text{opt}} = \alpha_0 (R/R_0) t, \quad (1)$$

$$d_B = \beta_0 (R/R_0)^{-1/2} t^{1/2}, \quad (2)$$

where the subscript “0” refers to the nominal case  $R = R_0$  at which the experiments presented in the previous section are performed. For the present materials we have  $F_{\text{opt}} \sim 5$  pN [35],  $\eta \sim 4$  mPa s, and  $T \sim 300$  K. The sorting time  $t_{\text{sort}}$  is therefore evaluated from the condition  $d_{\text{opt}} = L_0/2 + d_B$  [see Fig. 6(b)], which gives

$$t_{\text{sort}} = \left[ \frac{\beta_0}{2\alpha_0} \left( 1 + \sqrt{1 + \frac{2\alpha_0 L_0}{\beta_0^2} \left( \frac{R}{R_0} \right)^2} \right) \right]^2 \left( \frac{R}{R_0} \right)^{-3}. \quad (3)$$

The dependence of the sorting time on the particle size is shown in Fig. 6(c), choosing  $L_0 = 1$  mm for the sake of illustration and  $100 \text{ nm} < R < 100 \mu\text{m}$ , for which

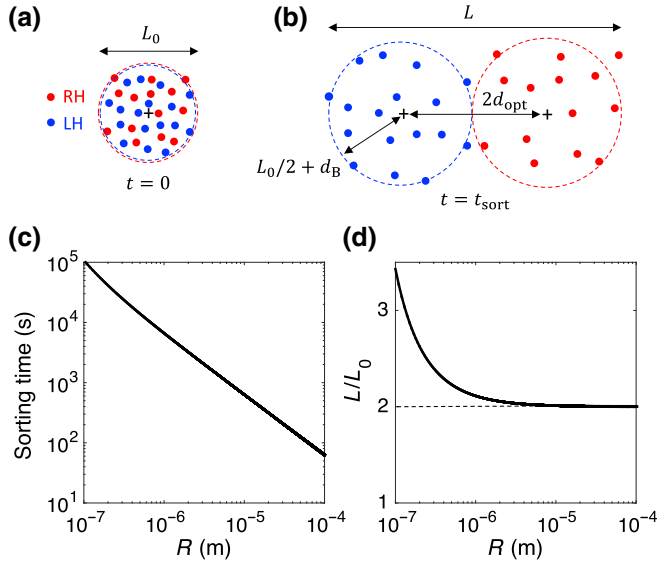


FIG. 6. (a),(b) The definition of the characteristic lengths used to evaluate the influence of the particle radius on the sorting time and the spatial extent of the racemic chiral particle assembly at  $t = t_{\text{sort}}$ . (c),(d) The sorting time  $t_{\text{sort}}$  and normalized size  $L/L_0$  of the particle assembly as a function of  $R$  for  $L_0 = 1$  mm (see text for details).

$0.1 \text{ fN} \lesssim F_{\text{opt}} \lesssim 0.1 \text{ nN}$ . The corresponding behavior for the spatial extent  $L$  of the sorted particles is shown in Fig. 6(d). A crossover between two regimes appears around the critical value  $R_c = R_0\beta_0/\sqrt{\alpha_0 L_0} \sim 10 - 100$  nm, above which the Brownian motion has little influence, as emphasized by the respective behavior  $t_{\text{sort}} \sim (L_0/\alpha_0)(R/R_0)^{-1}$  and  $L \sim 2L_0$ .

Nevertheless, we note that the strong reflectivity associated with the Bragg reflection and hence the magnitude of  $F_{\text{opt}}$  vanishes when the condition  $p \ll R$  is no longer satisfied, as is the case when  $R \lesssim 1 \mu\text{m}$ . This implies even larger sorting times for the smaller particles, which may prevent further developments using chiral-liquid-crystal droplets. However, optical enantioseparation does not aim at being restricted to cholesteric materials and a more generic evaluation is useful to provide a quantitative framework toward practical developments of optical enantioseparation techniques.

This is achieved by calculating the force (of any nature) exerted on individual particles in order to sort a given racemic assembly within a given time. This is done by combining the condition  $d_{\text{opt}} = L_0/2 + d_B$  at  $t = t_{\text{sort}}$  with Eqs. (1) and (2), which gives

$$F = \frac{6\pi\eta R}{t_{\text{sort}}} (\beta\sqrt{t_{\text{sort}}} + L_0/2). \quad (4)$$

The results are shown in Fig. 7, imposing a sorting time of 1 min, 1 h, or 1 d with  $L_0 = 1$  mm and  $\eta = 1$  mPa s.

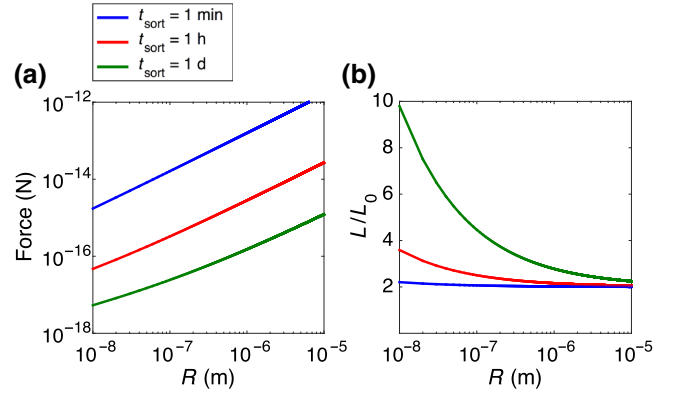


FIG. 7. (a) The force needed to sort a given racemic assembly as a function of the particle radius for three values of the sorting time. (b) The corresponding normalized spatial extent of the sorted assembly.

It appears that subfemtonewton-level discriminatory optical forces allow us to consider the enantioseparation of particles down to the nanoscale.

Another point is worth mentioning when dealing with enantioseparation in a fluidic environment, namely, the possible role played by hydrodynamic interactions, independent of the fact that fluids with low viscosity values are always to be welcomed. Indeed, every particle in motion generates long-range fluid flows around it. Such flows subsequently exert viscous forces on the surrounding particles. The resulting dynamics is that of a many-body system. In the recent years, collective motion of microparticles under optical fields has been unveiled as a valuable trick for studying nontrivial phenomena, such as pulling optical forces [41] and lateral optical forces [42], by benefiting from the hydrodynamic amplification effect. We thus expect to speed up the sorting process as the hydrodynamic interaction effects increase. This would be of interest when considering the provocative question of optical chiral resolution of nanometer-sized chiral particles or chiral molecular compounds. In the next section, we address this point numerically, for both 2D and 3D racemic emulsions under the action of a discriminatory force field.

## V. ENHANCED ENANTIOSEPARATION VIA HYDRODYNAMIC INTERACTION

Our simulations are based on a point-particle model, the robustness of which has been previously discussed in the context of the sedimentation of granular columns [43]. First, we randomly initialize the positions of  $N = 2M$  particles in a square (2D case) or cubic (3D case) box of characteristic length  $L_0$  given by  $\mathbf{r}_0^{(i)}$ , with  $i = (1, \dots, N)$ , in a Cartesian reference frame. Then, we assume that half the particles experience a force field along the  $x$  axis,  $F_x^{(i)} = F_0 f(x, y, z)$ , with  $F_0$  constant and  $i =$

(1, \dots, M), while the other half experience the opposite force field,  $F_x^{(i)} = -F_0 f(x, y, z)$ , with  $i = (M + 1, \dots, N)$ , where  $0 \leq f(x, y, z) \leq 1$  is the normalized force-field profile. Moreover, the inertial contribution is neglected and the dynamics of the particles are driven by the Stokes equation.

In the absence of interaction, the velocity vector field of each particle,  $\mathbf{v}^{(i)}$ , is therefore merely described by the Stokes velocity of a single particle under the force field,  $\mathbf{v}_0^{(i)} = \pm F_0 f(x, y, z)/(6\pi\eta R)\mathbf{x}$ , where  $\mathbf{x}$  is the  $x$ -axis unit vector and  $\eta$  is the dynamic viscosity of the surrounding fluid. Hydrodynamic interactions are described by adding a correction accounting for the flow generated by all other particles according to pairwise hydrodynamic interactions modeled by the dimensionless Green's function of the Stokes equation. Normalizing the velocity fields by  $v_0 = |F_0/(6\pi\eta R)|$ , the distances by  $L_0$ , and the time by  $\tau_0 = L_0/v_0$ , one obtains, for the normalized  $k$ -component,  $k = (x, y, z)$ , of the velocity field of the  $i$ th droplet

$$\mathbf{v}_k^{(i)} = f(x, y, z) \left[ \epsilon^{(i)} \delta_{xk} + \epsilon^{(j)} \frac{3R}{4L_0} \sum_{j \neq i} \left( \frac{\delta_{xk}}{D^{(ij)}} + \frac{D_x^{(ij)} D_k^{(ij)}}{D^{(ij)^3} \right) \right], \quad (5)$$

where  $\epsilon^{(n)} = +1$  for  $1 \leq n \leq M$  and  $\epsilon^{(n)} = -1$  for  $M + 1 \leq n \leq N$ . Also,  $\delta_{xk}$  refers to the Kronecker symbol and  $\mathbf{D}^{(ij)}$  is the normalized vector distance between the  $i$ th and  $j$ th particles. The resulting set of  $3N$  coupled differential equations for the positions of the particles given by  $d\mathbf{r}^{(i)}/dt = \mathbf{v}^{(i)}$ , and associated with the initial condition  $\mathbf{r}^{(i)}(t=0) = \mathbf{r}_0^{(i)}$ , is integrated using an Adams-Bashford algorithm. The single adjustable parameter is the ratio  $R/L_0$ , the value of which fixes the level of the hydrodynamic interactions.

Numerical simulations allow us to explore the boosting role of hydrodynamic interaction in both 2D and 3D. In the latter case, this is done by considering droplets with a random initial distribution in a cube of size  $R_0$ . An example is shown in Fig. 8, in the case of a uniform force field given by  $f(x, y) = 1$ , taking  $R/L_0 = 0.03$ . In the latter figure, the positions of the particles are shown at times  $t = (0, \tau_0/2, \tau_0)$  for  $N = 200$ . The effect of hydrodynamic interactions is clearly seen from the deformation of the initial clouds of right-handed and left-handed particles when the dynamics take place. The modifications, however, are substantially more significant along the force-field direction given by the  $x$  axis. The spatial redistribution of the particles is associated with curved trajectories in 3D as well as with the time and space dependence of the particles' velocity. Such behavior is addressed quantitatively by introducing a characteristic sorting time  $\tau$ , defined as

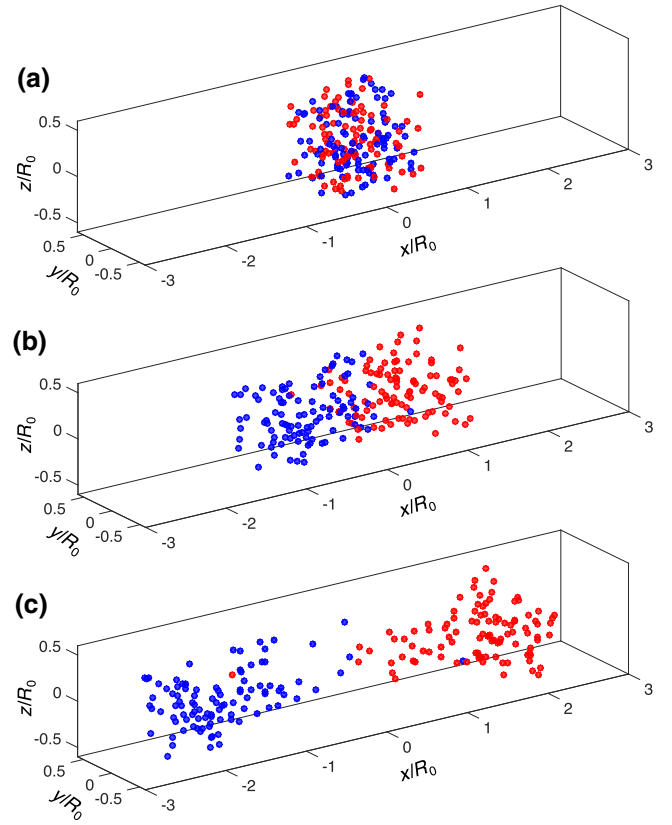


FIG. 8. The calculated positions of the particles for  $N = 200$  in the 3D case and for a uniform force field  $f = 1$ , at (a)  $t = 0$ , (b)  $t = \tau_0/2$ , and (c)  $t = \tau_0$ .

the minimal duration that ensures fulfillment of the condition  $|x_G^{\text{LH}}(\tau) - x_G^{\text{RH}}(\tau)| = L_0$ . Therefore, considering a uniform force field and uniformly distributed particles, the sorting time is constant in the absence of interaction,

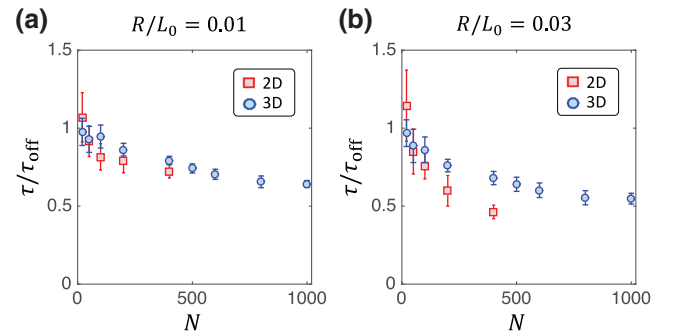


FIG. 9. The calculated reduced sorting time  $\tau/\tau_{\text{off}}$  for 2D and 3D racemic emulsions of chiral particles for a uniform force field characterized by  $f = 1$  as a function of the total number  $N$  of particles according to a purely viscous hydrodynamic interaction model described in the text. The reported values correspond to the average of ten independent simulation runs and the error bars refer to the standard deviation of the statistics.

$\tau_{\text{off}} = \tau_0/2$ , since the left-handed and right-handed populations move in opposite directions at the same velocity. In contrast, in presence of hydrodynamic interaction, the sorting time depends on the number of particles and on the magnitude of the interaction. This is demonstrated in Fig. 9, which presents a statistical study of the reduced sorting time  $\tau/\tau_{\text{off}}$  in the 2D and 3D cases, for a uniform force field and for two levels of hydrodynamic interaction, namely,  $R/L_0 = 0.01$  and  $R/L_0 = 0.03$ . Cooperative hydrodynamic effects actually decrease the sorting time all the more as their magnitude and the particle density increase.

## VI. CONCLUSION

To summarize, these results extend previous experimental attempts to observe discriminatory optical forces exerted on individual chiral objects by chiral light to many-body systems, where collective effects are prone to enhance sought-after chirality-selective sorting effects. By doing so, this work opens the way for further experimental implementation by considering particles with smaller sizes, toward the grail of all-optical resolution of chiral entities at the nanoscale. Finally, we note recent theoretical discussions on the possible use of a chiral light field endowed with chiral features that are not associated with the polarization state, as is the case for light fields carrying optical-phase singularities [44], which is another option through which to explore the experimental feasibility of alternative chiral optomechanics approaches.

## ACKNOWLEDGMENTS

This study has been carried out with financial support from the French National Research Agency (ANR) in the frame of the Investments for the future Programme IdEx Bordeaux LAPHIA (ANR-10-IDEX-03-02).

N.K. and A.A. contributed equally to this work.

- [1] L. Pasteur, Recherches sur les relations qui peuvent exister entre la forme cristalline, la composition chimique et le sens de la polarisation rotatoire, *Ann. Chim. Phys.* **24**, 442 (1848).
- [2] Lord Kelvin, The molecular tactics of a crystal, *J. Oxford Univ. Jr. Sci. Club* **18**, 3 (1894).
- [3] W. A. Bonner, Chirality and life, *Orig. Life Evol. Biosphere* **25**, 175 (1995).
- [4] J. Jacques, A. Collet, and S. H. Wilen, *Enantiomers, Racemates, and Resolutions* (Wiley-Interscience, New York, 1981).
- [5] E. L. Eliel and S. H. Wilen, *Stereochemistry of Organic Compounds* (Wiley-Interscience, New York, 1994).
- [6] G. Gübitz and M. G. Schmid, Chiral separation principles in chromatographic and electromigration techniques, *Mol. Biotechnol.* **32**, 159 (2006).
- [7] T. J. Ward and B. A. Baker, Chiral separations, *Anal. Chem.* **80**, 4363 (2008).
- [8] M. Avalos, R. Babiano, P. Cintas, J. L. Jiménez, J. C. Palacios, and L. D. Barron, Absolute asymmetric synthesis under physical fields: Facts and fictions, *Chem. Rev.* **98**, 2391 (1998).
- [9] W. Kuhn and E. Knopf, The preparation of optically active compounds by the aid of light, *Z. Phys. Chem.* **7**, 292 (1930).
- [10] K. L. Stevenson and J. F. Verdieck, Partial photoresolution. preliminary studies on some oxalato complexes of chromium (iii), *J. Am. Chem. Soc.* **90**, 2974 (1968).
- [11] H. Kagan, A. Moradpour, J. Nicoud, G. Balavoine, and G. Tsoucaris, Photochemistry with circularly polarized light: Synthesis of optically active hexahelicene, *J. Am. Chem. Soc.* **93**, 2353 (1971).
- [12] Y. Li, C. Bruder, and C. Sun, Generalized Stern-Gerlach Effect for Chiral Molecules, *Phys. Rev. Lett.* **99**, 130403 (2007).
- [13] B. Spivak and A. Andreev, Photoinduced Separation of Chiral Isomers in a Classical Buffer Gas, *Phys. Rev. Lett.* **102**, 063004 (2009).
- [14] X. Li and M. Shapiro, Theory of the optical spatial separation of racemic mixtures of chiral molecules, *J. Chem. Phys.* **132**, 194315 (2010).
- [15] A. Canaguier-Durand, J. A. Hutchison, C. Genet, and T. W. Ebbesen, Mechanical separation of chiral dipoles by chiral light, *New J. Phys.* **15**, 123037 (2013).
- [16] D. S. Bradshaw and D. L. Andrews, Chiral discrimination in optical trapping and manipulation, *New J. Phys.* **16**, 103021 (2014).
- [17] R. P. Cameron, S. M. Barnett, and A. M. Yao, Discriminatory optical force for chiral molecules, *New J. Phys.* **16**, 013020 (2014).
- [18] S. B. Wang and C. T. Chan, Lateral optical force on chiral particles near a surface, *Nat. Commun.* **5**, 3307 (2014).
- [19] D. Smith, C. Woods, A. Seddon, and H. Hoerber, Photophoretic separation of single-walled carbon nanotubes: A novel approach to selective chiral sorting, *Phys. Chem. Chem. Phys.* **16**, 5221 (2014).
- [20] A. Hayat, J. B. Mueller, and F. Capasso, Lateral chirality-sorting optical forces, *Proc. Ntl. Acad. Sci.* **112**, 13190 (2015).
- [21] M. H. Alizadeh and B. M. Reinhard, Transverse chiral optical forces by chiral surface plasmon polaritons, *ACS Photonics* **2**, 1780 (2015).
- [22] A. Canaguier-Durand and C. Genet, Plasmonic lateral forces on chiral spheres, *J. Opt.* **18**, 015007 (2016).
- [23] Y. Zhao, A. A. Saleh, and J. A. Dionne, Enantioselective optical trapping of chiral nanoparticles with plasmonic tweezers, *ACS Photon.* **3**, 304 (2016).
- [24] H. Chen, C. Liang, S. Liu, and Z. Lin, Chirality sorting using two-wave-interference-induced lateral optical force, *Phys. Rev. A* **93**, 053833 (2016).
- [25] I. D. Rukhlenko, N. V. Tepliakov, A. S. Baimuratov, S. A. Andronaki, Y. K. Gunko, A. V. Baranov, and A. V. Fedorov, Completely chiral optical force for enantioseparation, *Sci. Rep.* **6**, 36884 (2016).
- [26] T. Zhang, M. R. C. Mahdy, Y. Liu, J. H. Teng, C. T. Lim, Z. Wang, and C.-W. Qiu, All-optical chirality-sensitive sorting

- via reversible lateral forces in interference fields, *ACS Nano*, **11**, 4292 (2017).
- [27] P. Acebal, L. Carretero, and S. Blaya, Design of an optical conveyor for selective separation of a mixture of enantiomers, *Opt. Express* **25**, 32290 (2017).
- [28] T. Cao and Y. Qiu, Lateral sorting of chiral nanoparticles using fano-enhanced chiral force in visible region, *Nanoscale* **10**, 566 (2018).
- [29] G. Pellegrini, M. Finazzi, M. Celebrano, L. duò, M. A. Iati, O. M. Maragò, and P. Biagioni, Superchiral surface waves for all-optical enantiomer separation, arXiv:1803.10010 (2018).
- [30] R. J. Hernandez, A. Mazzulla, A. Pane, K. Volke-Sepulveda, and G. Cipparrone, Attractive-repulsive dynamics on light-responsive chiral microparticles induced by polarized tweezers, *Lab. Chip* **13**, 459 (2013).
- [31] G. Tkachenko and E. Brasselet, Spin Controlled Optical Radiation Pressure, *Phys. Rev. Lett.* **111**, 033605 (2013).
- [32] G. Tkachenko and E. Brasselet, Optofluidic chiral sorting of material chirality by chiral light, *Nat. Commun.* **5**, 3577 (2014).
- [33] G. Tkachenko and E. Brasselet, Helicity-dependent three-dimensional optical trapping of chiral microparticles, *Nat. Commun.* **5**, 4491 (2014).
- [34] M. Donato, J. Hernandez, A. Mazzulla, C. Provenzano, R. Saija, R. Sayed, S. Vasi, A. Magazzu, P. Pagliusi, R. Bartolino, P. Gucciardi, O. Marago, and G. Cipparrone, Polarization-dependent optomechanics mediated by chiral microresonators, *Nat. Commun.* **5**, 3656 (2014).
- [35] N. Kravets, A. Aleksanyan, and E. Brasselet, Chiral Optical Stern-Gerlach Newtonian Experiment, *Phys. Rev. Lett.* **122**, 024301 (2019).
- [36] J. Noh, H.-L. Liang, I. Drevensek-Olenik, and J. P. Lagerwall, Tuneable multicoloured patterns from photonic cross-communication between cholesteric liquid crystal droplets, *J. Mater. Chem. C* **2**, 806 (2014).
- [37] M. Faryad and A. Lakhtakia, The circular Bragg phenomenon, *Adv. Opt. Photonics* **6**, 225 (2014).
- [38] J. Bezic and S. Zumer, Structures of the cholesteric liquid crystal droplets with parallel surface anchoring, *Liq. Cryst.* **11**, 593-619 (1992).
- [39] D. Sec, T. Porenta, M. Ravnik, and S. Zumer, Geometrical frustration of chiral ordering in cholesteric droplets, *Soft Matter* **8**, 11982 (2012).
- [40] M. Humar and I. Musevic, 3D microlasers from self-assembled cholesteric liquid-crystal microdroplets, *Opt. Express* **18**, 26995 (2010).
- [41] V. Kajorndejnukul, W. Ding, S. Sukhov, C.-W. Qiu, and A. Dogariu, Linear momentum increase and negative optical forces at dielectric interface, *Nat. Photon.* **7**, 787 (2013).
- [42] S. Sukhov, V. Kajorndejnukul, R. R. Naraghi, and A. Dogariu, Dynamic consequences of optical spin-orbit interaction, *Nat. Photon.* **9**, 809 (2015).
- [43] H. Chraïbi and Y. Amarouchene, Sedimentation of granular columns in the viscous and weakly inertial regimes, *Phys. Rev. E* **88**, 042204 (2013).
- [44] I. A. Vovk, A. S. Baimuratov, W. Zhu, A. G. Shalkovskiy, A. V. Baranov, A. V. Fedorov, and I. D. Rukhlenko, Chiral nanoparticles in singular light fields, *Sci. Rep.* **7**, 45925 (2017).